TECHNICAL PAPER

The effect of build orientation on the mechanical properties of a variety of polymer AM-created triply periodic minimal surface structures

Abdurrahim Temiz[1]

Abstract

The advancements achieved in additive manufacturing (AM) have substantially transformed the design process of functional components. The change simplifies the fabrication of triply periodic minimal surface (TPMS) structures, whose unique geometric characteristics have garnered interest from numerous industries, including automotive, architecture, aerospace, and biomedical engineering. However, there is a scarcity of research in the literature about the investigation of the tensile mechanical properties of build orientation during the AM process of polymer-based TPMS. The objective of this study was to investigate the influence of three different types of TPMS structure and build orientations on the mechanical qualities of test specimens fabricated using masked stereolithography (MSLA) and a commercially accessible gray resin. Furthermore, the objective of the research was to determine the optimal TPMS pattern type and construct orientation in order to improve both elongation and ultimate tensile strength (UTS). A dog bone-shaped specimen was used for an experimental evaluation of their tensile properties. The test region was occupied by three different TPMS structures, namely the Gyroid (G), Schwarz Primitive (P), and Schwarz Diamond (D). The results showed that across all three building orientations, the D-shaped component produced the highest UTS, and the P-shaped component produced the largest elongation. The analysis of variance (ANOVA) results for UTS revealed that shape significantly influenced UTS by 83.11%, outweighing the 7.42% impact of construct orientation on UTS. Similarly, the ANOVA for elongation at break shows that build orientation (17.84%) had a substantially lower impact than shape (75.08%).

Keywords 3D printing · Cellular materials · Polymer additive manufacturing · Triply periodic minimal surface

1 Introduction

The term "additive manufacturing" (AM) is used to describe a group of manufacturing techniques that use a layer-by-layer approach to construct a part in its final or nearly final shape. When compared to traditional manufacturing processes, AM methods provide for greater design flexibility, which in turn allows for the production of complex, lightweight parts with enhanced functionality [1]. It has acquired widespread acceptance among manufacturers and academics over the last two decades due to its enormous potential for developing

and constructing sophisticated structures that would not be possible using traditional procedures [2]. A current trend in the design of AM components is to replace solid volumes with lightweight cellular structures for a variety of reasons, including increased energy efficiency and material use [1, 3]. A broad range of materials, from advanced engineering polymers to metals and ceramics, may be utilized in AM, which is categorized into seven process categories by the ASTM ISO 52900 nomenclature standard [4, 5]. Various AM techniques may be used to print with a wide variety of materials, including thermoplastic polymers, wax, ceramic, and many more [6]. Products with fine features and polished surfaces are well suited to vat photopolymerization (VP) methods of production. Most commonly, they are used in the medical and dental fields for things like hearing aids, face prosthetics, and surgical learning tools. By using an image of the required cross-section geometry and adjusting the intensity of the light shining on the photoresin, the VP approach

Technical Editor: Zilda de Castro Silveira.

✉ Abdurrahim Temiz
   abdurrahimtemiz@karabuk.edu.tr

1 Department of Industrial Design Engineering, Karabük University, Karabük, Turkey

is able to generate a variety of properties in a single material [7]. There are many distinct forms of VP, including as stereolithography (SLA) and digital light processing (DLP). The sole significant distinction among SLA, and DLP is in the curing process. DLP employs a digital light projector to cure an entire layer at once, whereas SLA employs a laser to cure the resin selectively layer by layer [8]. MSLA is a variant of SLA [9]. MSLA utilizes an LCD screen to conceal light and simultaneously cure an entire layer. Several previously machined components needed in the production of silicone molds for vacuum or injection molding may be replicated using SLA due to the technology's ability to create components with complicated geometries and surface finishes [10]. Despite the existence of other commercially accessible alternatives for SLA, it is widely acknowledged that this particular technique of three-dimensional (3D) printing serves as its foundational origin. SLA 3D printing is considered satisfactory in terms of speed, quality and build volume [11]. Due to the liquid-to-solid nature of the SLA technique, the mechanical properties of the material are subject to impact from several process parameters, ranging from the photopolymerization of the liquid resin through the post-curing phase. Mechanical characteristics of SLA-printed materials may be affected by build orientation, layer thickness, post-cure time, aging, supports, laser power, and the surrounding environment [12]. Among these factors, the build orientation of the component is crucial in additive manufacturing [13].

The discovery of new materials that are both lightweight and strong is of great scientific and technological interest because of the wide variety of engineering fields in which they may be put to use [14, 15]. Polymer foaming can form polymeric cellular structures using chemical [16] or physical [17] blowing agents. The results of these kinds of processes are typically unstable structures. Making polymeric cellular materials with 3D printing is another option. 3D printing enables the construction of complex architectural structures out of a wide variety of materials, and it provides exceptional control over the topologies and base materials of cellular structures [18]. The designer of a lattice structure faces a significant problem in determining which lattice design variables are most suitable for a given application [19]. Two methods for using minimum surfaces to generate lattices, one based on sheets and the other on ligaments or struts, were identified by [20]. In comparison with strut-based lattices (body-centered cubic, for example), which are more routinely produced and studied using AM, triply periodic minimal surface (TPMS) lattices were selected for this work due to their many potential benefits. TPMS are smooth, curved surfaces without any sharp corners or edges that divide space into two infinite, distinct regions [19, 21, 22]. The use of TPMS allows for the development of periodic composites and cellular structures with novel properties. The

mechanical properties of cellular structures can be modified to meet specific design needs, which is a major benefit [23]. The phases can be used efficiently in such composites [24]. Additionally, TPMS permits the development of cellular structures with a large surface area-to-volume ratio [25–27]. TPMS structures are unique designs of geometry that possess distinct mechanical properties, providing them a topic of significant scientific interest. Several studies have been conducted to investigate the mechanical characteristics and qualities of TPMS constructions. The work by Abueidda et al. [21] investigated the mechanical properties of 3D-printed polymeric Gyroid cellular structures, providing valuable insights into TPMS materials. In addition, the energy absorption, compressive strength, and uniaxial modulus of the Gyroid structures are compared to those of the IWP, Neovius, and Primitive structures, which were found in a previous study. When it comes to mechanical qualities, Gyroid structures are better than the other TPMS cellular structures. Peng et al. [28] studied 3D-printed sandwich beams with bioinspired cores, providing insights into the mechanical performance and modeling of TPMS structures. In brief, the findings of this work indicate that sandwich constructions incorporating TPMS cores had the potential to exhibit favorable flexural characteristics and provide effective energy absorption capabilities. In their study, Liang et al. [29] examined the deformation and energy absorption characteristics of cellular structures made of 3D-printed TPMS stainless steel. In contrast to the Primitive structure, which primarily extends and displays a substantial tension plateau, the Gyroid structure primarily bends and continues to harden. In contrast to the Primitive structure, the strain hardening of the Gyroid structure is more pronounced as a result of substantial geometric distortion and increased regions of spontaneous cell wall contact.

Design of experiment (DOE) allows for the systematic determination of the impact of design and process parameters. The number of tests needed to find the best mix of factors to improve the mechanical properties was cut down by using DOE. The Taguchi method was widely used by scientists to reduce the number of tests required for improving 3D printing process parameters [30].

This article compares the mechanical properties of three different types of TPMS cellular structures with the same density and cell size, all of which are manufactured from the same polymeric base material. SLA 3D-printed samples of Gyroid lattice (G), Schwarz Primitive lattice (P), and Schwarz Diamond lattice (P) structures were created for experimental characterization of their tensile properties. Manufacturing was conducted in three various building orientations (on edge, upright, and flat), and the effect of each was analyzed. In order to achieve this goal, the Taguchi method was employed to determine parameters and their levels in each run. The findings were also analyzed using the analysis of variance (ANOVA)

test. The tensile qualities of TPMS structures have not been the focus of much previous research; thus, this one was undertaken to fill that gap.

2 Materials and methods

2.1 Design of sheet-based architectural TPMS

As the tensile test specimen for the ASTM D638 standard [31], a dog bone was utilized, and the patterns were positioned inside the test region. SpaceClaim is a part of computer-aided design (CAD) and computer-aided engineering (CAE) software that is integrated into the array of simulation and analysis tools offered by ANSYS. The dimensions of the specimen were taken from a Type IV model, and the CAD was created in a SpaceClaim environment. The dimensions of the Type IV dog bone model are depicted in Fig. 1. The thickness of the specimens is 3.2 mm.

SpaceClaim was used to create designs for tree-distinctive sheet-based TPMS (Gyroid lattice, Schwarz Primitive lattice, and Schwarz Diamond lattice). The unit cell of one of these lattices is illustrated in Fig. 2. These lattices are generated and developed analytically utilizing level-set approximation equations [22]. The equations for the level-set approximation can be written as:

$$f(x, y, z) = c \tag{1}$$

where c is the level-set parameter, $x = 2nX/L$, $y = 2nY/L$, and $z = 2nZ/L$, where n is the number of unit cells (i.e., periodicity), L is the structure size, and X, Y, and Z are the Cartesian coordinate systems. The wall thickness of the TPMS structures was determined parametrically when the infill rate was 20% and the cell length was 3.2 mm. Each building had the same cell count and infill ratio but had distinctive wall thicknesses. It is possible to build arbitrary G, D, and P lattice structures with arbitrary cell counts and volume fractions by solving the TPMS equations for the $U = 0$ isosurface [19].

$$U_G = \cos(k_x x)\sin(k_y y) + \cos(k_y y)\sin(k_z z) + \cos(k_z z)\sin(k_x x) - t, \tag{2a}$$

$$U_P = \cos(k_x x) + \cos(k_y y) + \cos(k_z z) - t, \tag{2b}$$

$$U_D = \sin(k_x x)\sin(k_y y)\sin(k_z z) + \sin(k_x x)\cos(k_y y)\cos(k_z z)$$
$$+ \cos(k_x x)\sin(k_y y)\cos(k_z z) + \cos(k_x x)\cos(k_y y)\sin(k_z z) - t, \tag{2c}$$

and thinking of this interface as the solid-void transition zone. In Eqs. (2a)–(2c), t is a variable that can be used to adjust the volume fraction, ρ, of the resulting lattice. The following expressions can be written in terms of the periodicities of the TPMS functions, denoted by

$$k_i = 2\pi \frac{n_i}{L_i} (\text{with} i = x, y, z), \tag{3a}$$

where n_i represents the number of cell repeats in x, y, and z, and L_i represents the absolute sizes of the structure in those axes.

2.2 Taguchi design of experiments

The Taguchi technique is a statistically effective approach that aims to determine the optimal operating condition settings with minimal testing. By utilizing this method, researchers may reduce both the time and cost associated with conducting experiments [32]. One of the primary benefits of employing the Taguchi technique for optimization lies in the utilization of orthogonal arrays (OAs) for design, which effectively streamlines the process of experiment planning. Taguchi designs acknowledge the inherent limitation of controlling all aspects that contribute to
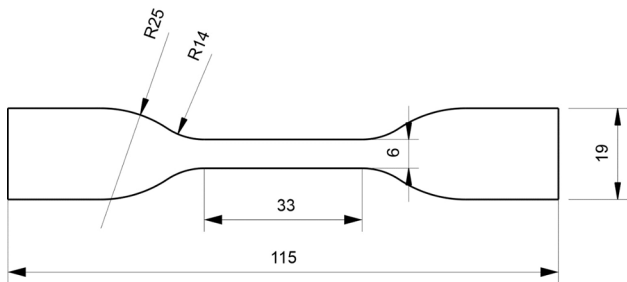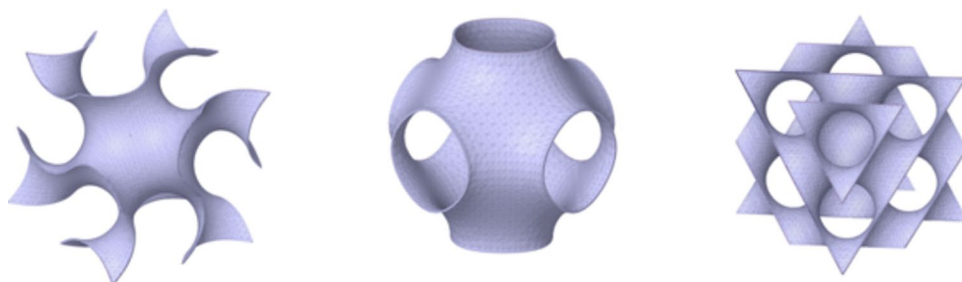

Fig. 1 Geometry of the test specimens was determined in accordance with the specifications provided in ASTM D638-14 (all dimensions in mm) [31]

Fig. 2 Unit cell of different sheet-based TPMS

unpredictability. The factors that cannot be controlled are sometimes referred to as noise factors. This study employed a full factorial design of two factors, each with three levels. The primary objective of employing a Taguchi full factorial design, comprising two factors with three levels each, is to systematically investigate the potential interactions and impacts of these factors on a certain response or output in a manner that is both efficient and comprehensive. The parameters that are hypothesized to have an impact on UTS and elongation at break include the type of TPMS pattern and the orientations used in the manufacturing process. Table 1 presents a visual representation of the factors that were taken into account, along with their corresponding levels.

Minitab's L9 Taguchi's orthogonal array was used to generate the main effects plot for the signal-to-noise (*S/N*) ratio graphs of mechanical characteristics. The *S/N* ratio quantifies the degree to which actual output deviates from the expected or nominal value. *S/N* ratios are classified into three categories: smaller is better, larger is better, and nominal is better [33]. Because the goal of this study is to increase tensile strength and elongation, the larger is better characteristic was selected, which employs Eq. (1):

$$S/N = -10\log_{10}\left[\frac{1}{n}\sum_{i=1}^{n}\frac{1}{y_i^2}\right] \qquad (4a)$$

### 2.3 Additive manufacturing of TPMS lattices

An Anycubic Photon Mono SE MSLA system with a light source (405 nm) was used in this work. The Anycubic Photon Mono SE printing equipment has a build volume of 130 mm × 78 mm × 160 mm. The printers use an LCD screen to provide a masked picture of the sliced data and a 405 nm Para LED matrix as the UV light source. Printing at a layer height of 0.01–0.15 mm with an *XY* precision of 0.051 mm, a *Z* resolution of 0.01 mm, and a build speed of 80 mm/h is possible because of the UV light source. Anycubic standard UV Resin was utilized for this investigation. The Standard UV resin is a UV-curable resin that cures at a UV curing wavelength of 365–410 nm and a typical exposure period of 5–15 s, making it ideal for precise applications. Table 2 lists the properties of the UV resin used.

The Anycubic Standard Gray UV resin is a frequently employed substance in the field of 3D printing. This resin has been formulated with the explicit purpose of being

Table 1 Levels of the factors

Factors	Levels		
TPMS pattern types	G	P	D
Build orientations	Upright	Flat	On edge

Table 2 Properties of a standard UV resin

Properties	Value
Density (g/cm^3)	1.05–1.25
Viscosity (cP or mPa·s)	150–200
Molding shrinkage (%)	3.72–4.24
Surface hardness (HD)	84
Flexural strength (MPa)	50–70
Tensile strength (MPa)	36–52
Flexural modulus (MPa)	1,200–1,600

compatible with SLA 3D printers, such as the Anycubic Photon Mono *X* and Photon Mono SE models [34]. The process of SLA technology involves the utilization of a monomer compound that is combined with a photo-initiator substance. This combination enables the creation of solid objects through a layer-by-layer approach [35]. The Anycubic Standard Gray UV resin exhibits compatibility with the mentioned printers and demonstrates remarkable mechanical performance [36]. It also exhibits versatility in its applicability, encompassing a diverse array of uses such as prototyping, model fabrication, and even dental restorations [37]. The resin possesses the capability to generate complex structures encompassing many geometrical forms [38]. The ASTM D638 standard test protocol for determining the tensile properties of polymers was adhered to in order to produce a dog bone tensile test specimen [31]. Tensile test specimens were printed with a layer thickness of 0.5 mm, an exposure length of 5 s, and in a variety of build orientations (on edge, upright, and flat). Figure 3 presents a schematic representation of printed samples pertaining to diverse areas of building construction. The automatic support mode was utilized to generate the on-edge specimen, as certain surfaces were not in touch with the table and required additional support. Following the DOE parameter combination, nine distinct samples were successfully printed. Parameters and
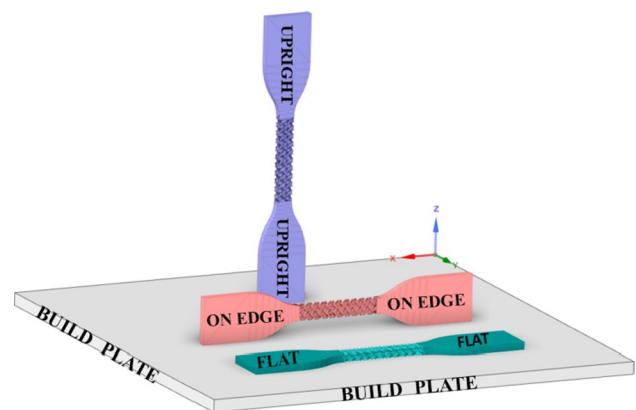
Fig. 3 Images of printed samples from various building orientations

their levels for each run were determined using the Taguchi technique.

2.4 Mechanical testing

The AG-50 kN Shimadzu Autograph was used to conduct the tensile test at a constant crosshead speed of 5 mm/min and room temperature. Indirectly validating the suitability of utilizing a 50 kN load cell to conduct such tests are additional sources that provide valuable insights into the mechanical properties and testing protocols of polymer materials [39, 40]. Tensile tests were conducted in accordance with the guidelines outlined in ASTM D638 [31]. The samples were subjected to tensile testing until they were broken. Figure 4 depicts a tensile test of a sample. To reduce the influence of variations and random error sources, up to three copies of each specimen were produced for each planned experiment. The specimens underwent a maximum of three printings and evaluations per intended experiment to minimize the impact of random changes and potential sources of error.

3 Result and discussion

This section presents and evaluates the mechanical response derived from tensile tests of three minimal surfaces with different build orientations. Tensile tests were used to determine the UTS and elongation at break. Each measurement was averaged over the repeated specimens, and the mean findings with standard deviations are shown in Table 3. In this study, the letters G, P, and D stand for the Gyroid lattice, the Schwarz Primitive lattice, and the Schwarz Diamond lattice, respectively. Tensile strengths peak at 1.50 MPa for run 4 and drop to 0.70 MPa for run 7. In addition, run 5 has the most elongation at the break (9.49%), and run 9 has

Fig. 4 A tensile test sample being tested

**Table 3** DOE with L9 Taguchi orthogonal array and results of the tensile tests

Runs	Shape	Orientation	UTS (MPa) (±SD)	Elongation (%) (±SD)
1	G	Upright	1.10±0.23	4.96±0.21
2	G	Flat	1.13±0.14	7.75±0.57
3	G	On edge	0.88±0.12	5.68±0.17
4	P	Upright	0.70±0.25	7.63±0.33
5	P	Flat	1.02±0.13	9.49±0.79
6	P	On edge	0.81±0.21	7.99±0.82
7	D	Upright	1.50±0.30	4.99±1.07
8	D	Flat	1.40±0.06	5.09±0.71
9	D	On edge	1.34±0.35	4.09±0.49

the lowest (4.09%). These findings suggest that the optimal shape for elongation is P, while the optimal shape for UTS is D. In order to enhance the clarity of these findings, Table 4 presents descriptive statistics. In addition to the maximum and minimum values, this dataset also includes the average values, standard error of the mean, coefficient of variation (CV), and the values for the first and third quartiles. The CV for UTS is 25.10, indicating that the standard deviation is a substantial fraction of the mean. This observation implies that the data obtained from UTS has a considerable degree of variation. The CV for elongation is calculated to be 28.73, suggesting a considerably elevated level of variability in comparison with the mean. The data on elongation likewise exhibits a significant degree of dispersion around the average value. In all instances, a CV over 20–30% might be regarded as relatively elevated, suggesting substantial variability within the dataset. The findings suggest that these parameters have a considerable impact on both UTS and elongation.

Figure 5 depicts stress–strain curves for samples of the same shape but built in different orientations. Figure 6 depicts the stress–strain curves for three type-shaped samples with the same build orientations. As seen from the stress–strain curves, the TPMS-shaped curves of the samples show a transition from low stress to considerable strain, an elastic deformation stage at the start of the deformation process, and a relatively long plateau stage. The outcomes presented here are consistent with the conclusions drawn from the extant body of literature [21, 23, 29]. When looking at all three figures in Fig. 5, it becomes clear that the upright build orientation yielded the lowest UTS. The following discussion explains why this conclusion agrees with the published research. The print layer is perpendicular to the applied force; hence, the failure load is lowest for an upright build orientation. When constructed parallel to the tensile tension, the bonding was flexible but robust [13]. Consistent with previous research, it was found that using materials on

**Table 4** Presentation of descriptive statistics

Variables	N	Mean	SE mean	CV	Min	Q1	Q3	Max
UTS	9	1.09 MPa	0.09	25.10	0.70 MPa	0.84	1.37	1.50 MPa
Elongation	9	6.41%	0.61	28.73	4.09%	4.97	7.87	9.49%
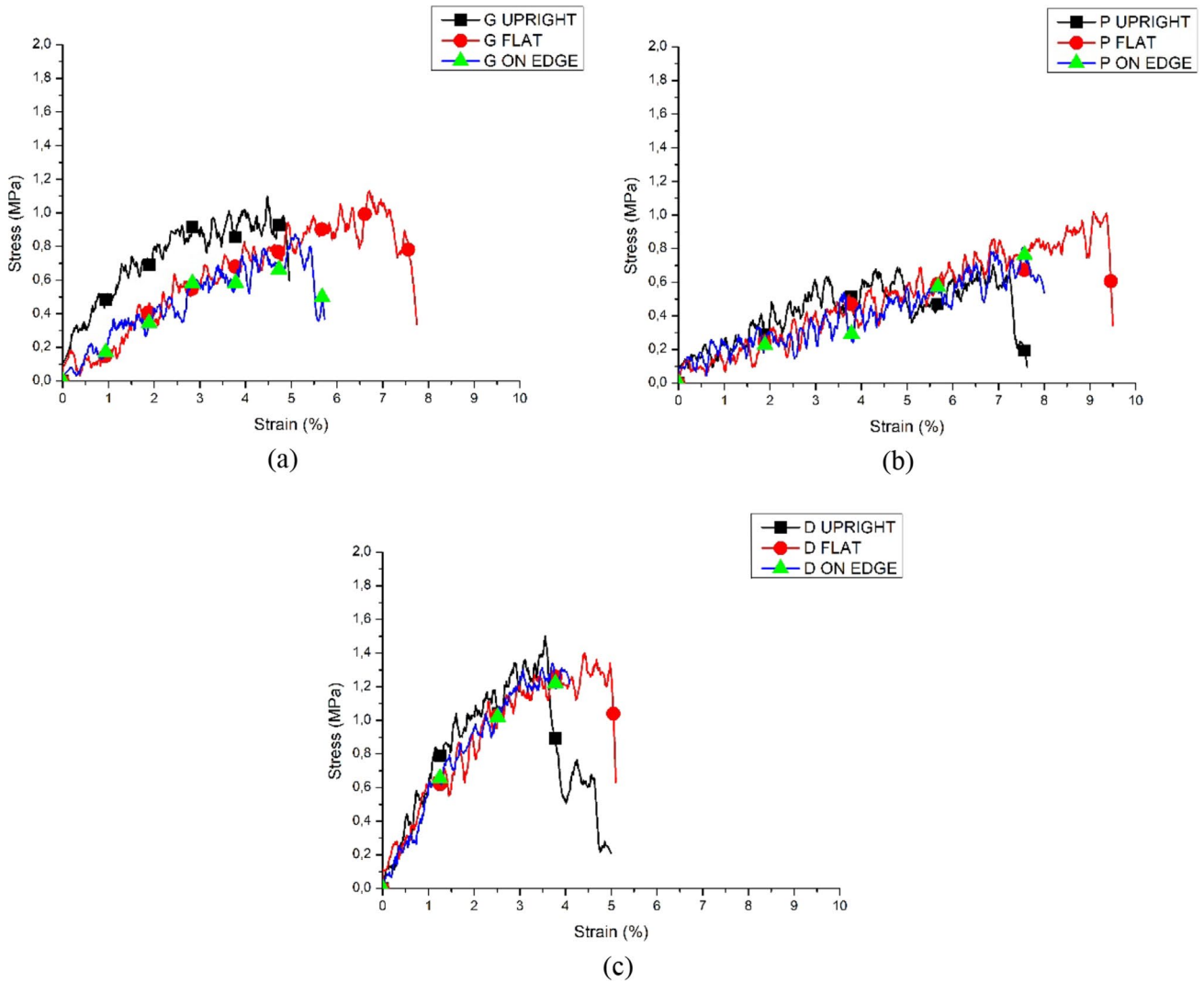
Fig. 5 Stress–strain curves **a** G shape with different built orientation, **b** P shape with different built orientations and **c** D shape with different built orientations

both sides of the support for the SLA-printed part reduced its tensile strength by 3.9% compared to using materials on only one side of the support [41]. Figure 6 shows that the D-shaped part yielded the highest UTS across all three building orientations, whereas the P-shaped part yielded the greatest elongation. In contrast to the Primitive structure, which, akin to the findings in the literature, predominantly undergoes elongation and demonstrates a notable stress plateau, the Gyroid structure primarily undergoes bending and indicates a continued increase in stiffness [29].

Figure 7 depicts the consequences of changing parameters affecting UTS and elongation at break using the Taguchi design method. The highest S/N ratio gives the finest levels for running parameters in S/N ratio figures. The appropriate factor levels for UTS were defined in the image by taking the D shape and flat-constructed orientation into account. "A3–B2" is the optimal combination of factors for UTS. The best value of elongation at the break was obtained with a P shape and a flat-built orientation. Elongation at break is best optimized by the "A2–B2" combination of parameters.
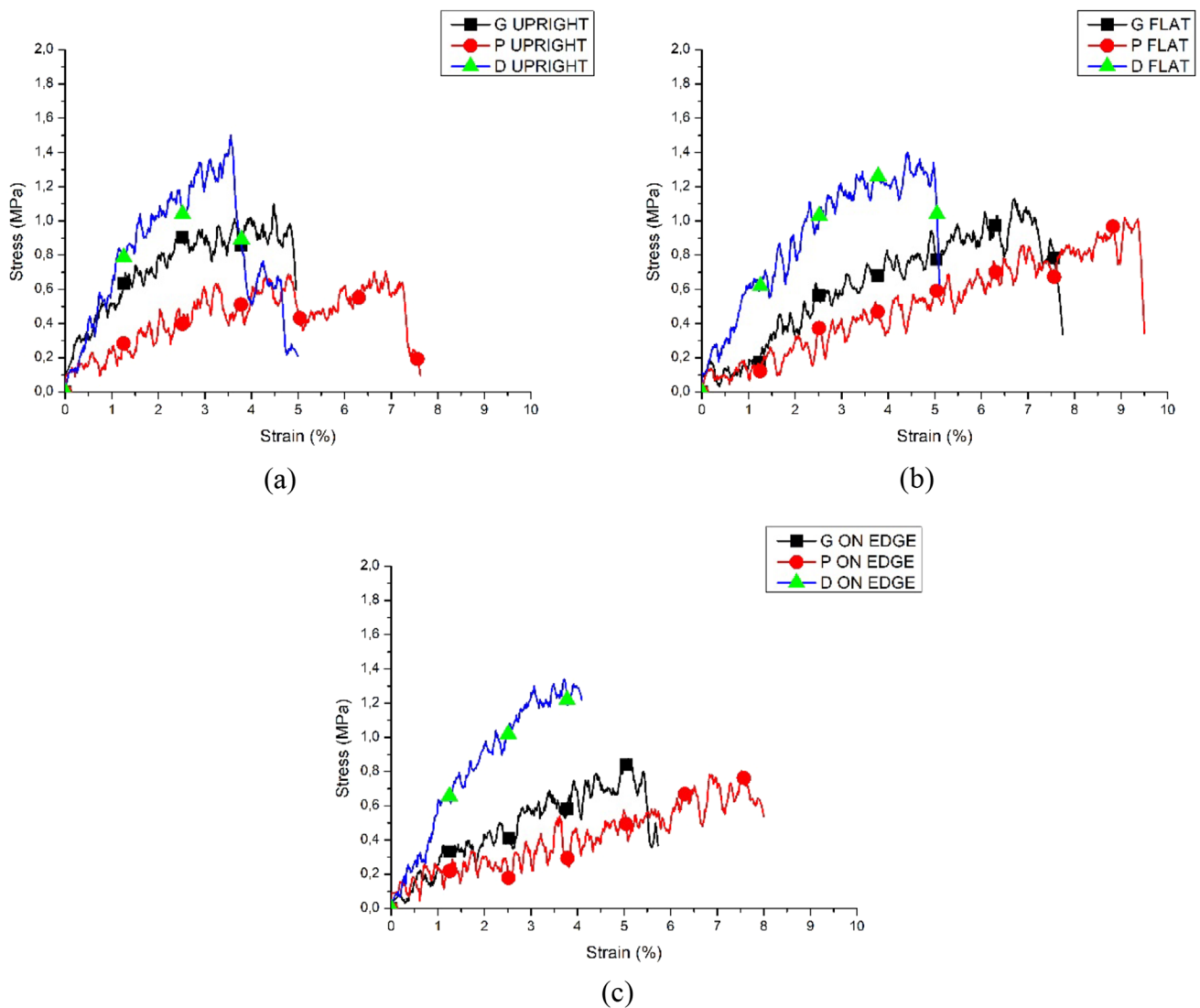
Fig. 6 Stress–strain curves **a** upright built orientation with different shapes, **b** flat-built orientation with different shapes and **c** on-edge-built orientation with different shapes

Table 5's ANOVA for UTS shows that the influence of shape on UTS was 83.11%, which was significantly higher than the effect of build orientation on UTS (7.42%). Similarly, the effect of shape (75.08%) on elongation at break was quite high as compared to build orientation (17.84%), as seen in Table 6's ANOVA for elongation. It is generally agreed that a p-value of 0.05 or above renders a model useless. If the p-value of a component is less than 0.05, it is highly likely that the factor had a major influence on the final model [30, 42]. The p-values for the linear coefficients of shape for UTS and elongation at break are less than 0.05, as shown in Tables 5 and 6. However, both UTS and elongation at break have p-values for build orientation that are more than 0.05. It can be concluded that both shape and build orientation influence UTS optimization. Shape, on the other hand, is a very effective criterion for both UTS and elongation at the break. This result is consistent with the findings in Figs. 5 and 6. The R^2 coefficient of determination was also used in a numerical technique for model validation. Values of R^2 close to 1 indicate a high degree of agreement between the experimental and model findings [30]. The R^2 values for UTS and elongation at break are 90.43 and 92.92%, respectively, as shown in Table 5 and 6. Estimation of R^2 values of 51.56 and 64.15 were determined for UTS and elongation at break, respectively. The R^2 values demonstrate the model's accuracy; however, it can be seen that the numbers are quite far from 1 for estimation.
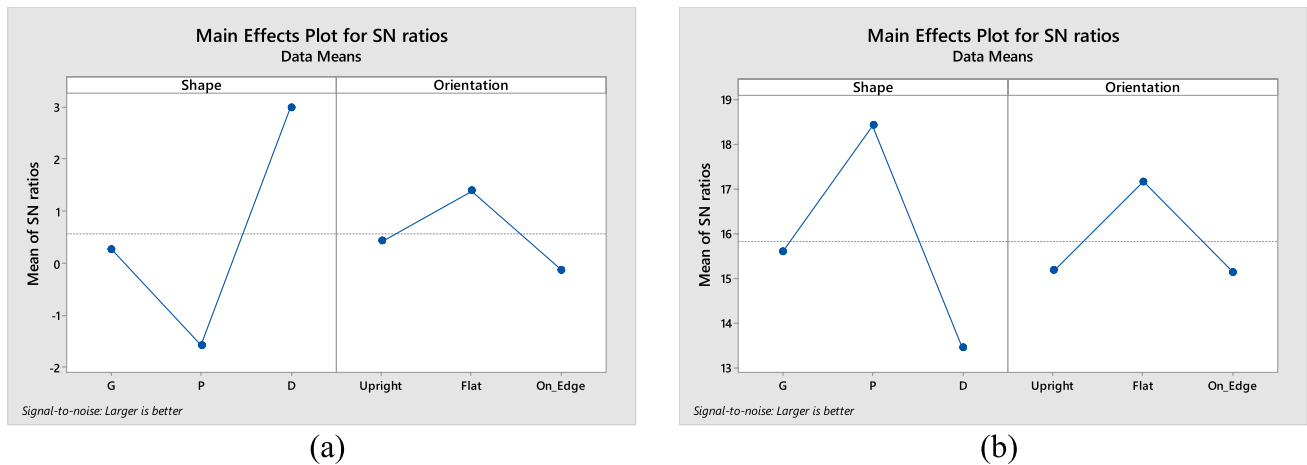
Fig. 7 *S/N* values of factor levels for **a** UTS, and **b** elongation at break

Table 5 ANOVA for UTS

Source	UTS			
	DF	Contribution	*F*-value	*p*-value
Shape	2	83.01%	17.35	0.011
Orientation	2	7.42%	1.55	0.317
Error	4	9.57%		
Total	8	100,00%		
R^2	90.43%			
Adj. R^2	80.86%			
Pred. R^2	51.56%			

Table 6 ANOVA for elongation at break

Source	UTS			
	DF	Contribution	*F*-value	*p*-value
Shape	2	75.08%	21.20	0.007
Orientation	2	17.84%	5.04	0.081
Error	4	7.08%		
Total	8	100.00%		
R^2	92.92%			
Adj. R^2	85.84%			
Pred. R^2	64.15%			

4 Conclusions

This study compared the mechanical characteristics of test specimens fabricated from MSLA and a commercially available gray resin using a variety of TPMS model types and structure orientations. The research was also conducted to find out which TPMS pattern type and build orientation would improve UTS and elongation at break the most. Production outcomes were evaluated for on-edge, upright, and flat-building configurations. The results demonstrated that the D-shaped component generated the highest UTS across all three building orientations, whereas the P-shaped component generated the largest elongation. The results clearly show that the minimum UTS was obtained when the subject was produced in the upright position. The flat-constructed orientation has a lower UTS and elongation at break than the on-edge manufactured orientation. This distinction is likely attributable to the production-stage supports. It is speculated that the supports degrade the areas around them. The impact of shape on UTS was 83.11 percent, according to an ANOVA for UTS, which is considerably larger than the 7.42 percent impact of build orientation on UTS. Likewise, the ANOVA for elongation at break reveals that the effect of shape (75.08%) on elongation at break was significantly greater than that of construct orientation (17.84%).

References

1. Hassan IM, Enab TA, Fouda N, Eldesouky I (2023) Design, fabrication, and evaluation of functionally graded triply periodic minimal surface structures fabricated by 3D printing. J Braz Soc Mech Sci Eng 45:66. https://doi.org/10.1007/s40430-022-03972-3
2. Majeed M, Khan HM, Wheatley G, Situ R (2022) Influence of post-processing on additively manufactured lattice structures. J Braz Soc Mech Sci Eng 44:389. https://doi.org/10.1007/s40430-022-03703-8
3. Kim WR, Bang GB, Kwon O et al (2020) Fabrication of porous pure titanium via selective laser melting under low-energy-density process conditions. Mater Des 195:109035. https://doi.org/10.1016/j.matdes.2020.109035

4. du Plessis A, Razavi N, Benedetti M et al (2022) Properties and applications of additively manufactured metallic cellular materials: a review. Prog Mater Sci 125:100918. https://doi.org/10.1016/j.pmatsci.2021.100918

5. ASTM ISO 52900: Additive manufacturing—General principles—Fundamentals and vocabulary. Standard (2021), American Society for Testing Materials, West Conshohocken

6. Bhosale V, Gaikwad P, Dhere S et al (2022) Analysis of process parameters of 3D printing for surface finish, printing time and tensile strength. Mater Today Proc 59:841–846. https://doi.org/10.1016/j.matpr.2022.01.210

7. Leben LM, Schwartz JJ, Boydston AJ et al (2018) Optimized heterogeneous plates with holes using 3D printing via vat photopolymerization. Addit Manuf 24:210–216. https://doi.org/10.1016/j.addma.2018.09.018

8. Pagac M, Hajnys J, Ma Q-P et al (2021) A review of vat photopolymerization technology: materials, applications, challenges, and future trends of 3D printing. Polymers 13:598. https://doi.org/10.3390/polym13040598

9. Ligon SC, Liska R, Stampfl J et al (2017) Polymers for 3D printing and customized additive manufacturing. Chem Rev 117:10212–10290. https://doi.org/10.1021/acs.chemrev.7b00074

10. Upcraft S, Fletcher R (2003) The rapid prototyping technologies. Assem Autom 23:318–330. https://doi.org/10.1108/01445150310698634

11. Phillips BT, Allder J, Bolan G et al (2020) Additive manufacturing aboard a moving vessel at sea using passively stabilized stereolithography (SLA) 3D printing. Addit Manuf 31:100969. https://doi.org/10.1016/j.addma.2019.100969

12. Wang S, Ma Y, Deng Z et al (2020) Implementation of an elastoplastic constitutive model for 3D-printed materials fabricated by stereolithography. Addit Manuf 33:101104. https://doi.org/10.1016/j.addma.2020.101104

13. Saini J, Dowling L, Kennedy J, Trimble D (2020) Investigations of the mechanical properties on different print orientations in SLA 3D printed resin. Proc Inst Mech Eng C J Mech Eng Sci 234:2279–2293. https://doi.org/10.1177/0954406220904106

14. Gibson LJ, Ashby MF (1999) Cellular solids: structure and properties, 2nd edn. Cambridge University Press, Cambridge, UK

15. Fleck NA, Deshpande VS, Ashby MF (2010) Micro-architectured materials: past, present and future. Proc R Soc A Math Phys Eng Sci 466:2495–2516. https://doi.org/10.1098/rspa.2010.0215

16. Bledzki AK, Faruk O (2006) Microcellular injection molded wood fiber-PP composites: part I—effect of chemical foaming agent content on cell morphology and physico-mechanical properties. J Cell Plast 42:63–76. https://doi.org/10.1177/0021955X06060945

17. Taki K, Yanagimoto T, Funami E et al (2004) Visual observation of CO_2 foaming of polypropylene-clay nanocomposites. Polym Eng Sci 44:1004–1011. https://doi.org/10.1002/pen.20093

18. Abueidda DW, Bakir M, Abu Al-Rub RK et al (2017) Mechanical properties of 3D printed polymeric cellular materials with triply periodic minimal surface architectures. Mater Des 122:255–267. https://doi.org/10.1016/j.matdes.2017.03.018

19. Maskery I, Sturm L, Aremu AO et al (2018) Insights into the mechanical properties of several triply periodic minimal surface lattice structures made by polymer additive manufacturing. Polymer 152:62–71. https://doi.org/10.1016/j.polymer.2017.11.049

20. Kapfer SC, Hyde ST, Mecke K et al (2011) Minimal surface scaffold designs for tissue engineering. Biomaterials 32:6875–6882. https://doi.org/10.1016/j.biomaterials.2011.06.012

21. Abueidda DW, Elhebeary M, Shiang (Andrew) C-S et al (2019) Mechanical properties of 3D printed polymeric Gyroid cellular structures: experimental and finite element study. Mater Des 165:107597. https://doi.org/10.1016/j.matdes.2019.107597

22. Abou-Ali AM, Al-Ketan O, Lee D-W et al (2020) Mechanical behavior of polymeric selective laser sintered ligament and sheet based lattices of triply periodic minimal surface architectures. Mater Des 196:109100. https://doi.org/10.1016/j.matdes.2020.109100

23. Temiz A, Yaşar M, Koç E (2022) Fabrication of open-pore biodegradable magnesium alloy scaffold via infiltration technique. Int Metalcast 16:317–328. https://doi.org/10.1007/s40962-021-00604-9

24. Dalaq AS, Abueidda DW, Abu Al-Rub RK, Jasiuk IM (2016) Finite element prediction of effective elastic properties of interpenetrating phase composites with architectured 3D sheet reinforcements. Int J Solids Struct 83:169–182. https://doi.org/10.1016/j.ijsolstr.2016.01.011

25. Yoo D-J (2014) Advanced porous scaffold design using multi-void triply periodic minimal surface models with high surface area to volume ratios. Int J Precis Eng Manuf 15:1657–1666. https://doi.org/10.1007/s12541-014-0516-5

26. Mulhi A, Dehgahi S, Waghmare P, Qureshi A (2023) Dimensional assessment of uniformly periodic porosity primitive TPMS lattices using additive manufacturing laser powder bed fusion technique. Int J Adv Manuf Technol 124:2127–2148. https://doi.org/10.1007/s00170-022-10578-5

27. Temiz A, Alshemary AZ, Akar N, Yaşar M (2023) Rapid casting of biodegradable porous magnesium scaffolds and electrophoretic deposition of 45S5 bioactive glass nanoparticles coatings on porous scaffolds: characterization and in vitro bioactivity analysis. Int Metalcast 17:1871–1882. https://doi.org/10.1007/s40962-022-00903-9

28. Peng C, Fox K, Qian M et al (2021) 3D printed sandwich beams with bioinspired cores: mechanical performance and modelling. Thin-Walled Struct 161:107471. https://doi.org/10.1016/j.tws.2021.107471

29. Liang Y, Zhou W, Liu Y et al (2021) Energy absorption and deformation behavior of 3D printed triply periodic minimal surface stainless steel cellular structures under compression. Steel Res Int 92:2000411. https://doi.org/10.1002/srin.202000411

30. Temiz A (2023) The effects of process parameters on tensile characteristics and printing time for masked stereolithography components, analyzed using the response surface method. J Mater Eng Perform. https://doi.org/10.1007/s11665-023-08617-7

31. ASTM D638—14: standard test method for tensile properties of plastics. Standard (2015), American Society for Testing Materials, West Conshohocken

32. Uslu S, Aydın M (2020) Effect of operating parameters on performance and emissions of a diesel engine fueled with ternary blends of palm oil biodiesel/diethyl ether/diesel by Taguchi method. Fuel 275:117978. https://doi.org/10.1016/j.fuel.2020.117978

33. Demir S, Yüksel C (2022) Evaluation of effect and optimizing of process parameters for fused deposition modeling parts on tensile properties via Taguchi method. Rapid Prototyp J 29:720–730. https://doi.org/10.1108/RPJ-06-2022-0201

34. Solyaev YO, Ustenko AD, Babaytsev AV, Dobryanskiy VN (2023) Improved mechanical performance of quasi-cubic lattice metamaterials with asymmetric joints. Sci Rep 13:14846. https://doi.org/10.1038/s41598-023-41614-3

35. Komjaty A, Wisznovszky (Muncut) ES, Culda LI (2021) Study on the influence of technological parameters on 3D printing with sla technology. MATEC Web Conf 343:01003. https://doi.org/10.1051/matecconf/202134301003

36. Rosace G, Palucci Rosa R, Arrigo R, Malucelli G (2021) Photosensitive acrylates containing bio-based epoxy-acrylate soybean oil for 3D printing application. J Appl Polym Sci 138:51292. https://doi.org/10.1002/app.51292

37. Soto-Montero J, de Castro EF, de Romano BC et al (2022) Color alterations, flexural strength, and microhardness of 3D printed resins for fixed provisional restoration using different post-curing

times. Dent Mater 38:1271–1282. https://doi.org/10.1016/j.dental.2022.06.023

38. Kiyotake EA, Thomas EE, Homburg HB et al (2022) Conductive and injectable hyaluronic acid/gelatin/gold nanorod hydrogels for enhanced surgical translation and bioprinting. J Biomed Mater Res Part A 110:365–382. https://doi.org/10.1002/jbm.a.37294

39. Mishra AK, Chavan H, Kumar A (2021) Effect of material variation on the uniaxial compression behavior of FDM manufactured polymeric TPMS lattice materials. Mater Today Proc 46:7752–7759. https://doi.org/10.1016/j.matpr.2021.02.276

40. Wittbrodt B, Pearce JM (2015) The effects of PLA color on material properties of 3-D printed components. Addit Manuf 8:110–116. https://doi.org/10.1016/j.addma.2015.09.006

41. Kazemi M, Rahimi AR (2015) Supports effect on tensile strength of the stereolithography parts. Rapid Prototyp J 21:79–88. https://doi.org/10.1108/RPJ-12-2012-0118

42. Simsek S, Uslu S (2020) Determination of a diesel engine operating parameters powered with canola, safflower and waste vegetable oil based biodiesel combination using response surface methodology (RSM). Fuel 270:117496. https://doi.org/10.1016/j.fuel.2020.117496